Journal of Materials Chemistry A

Promoting inherent catalytic activity and stability of TiO_2 supported Pt single-atoms at CeO_x-TiO_2 interfaces

Journal:	*Journal of Materials Chemistry A*
Manuscript ID	TA-ART-09-2021-008059
Article Type:	Paper
Date Submitted by the Author:	19-Sep-2021

Complete List of Authors:	Yoo, Mi; Chungnam National University, Materials Science & Engineering Kang, Eunji; Chungnam National University, Department of Nanomaterials Engineering Choi, Hyuk ; Chungnam National University, Materials science and Engineering Ha, Hyunwoo; Chungnam National University, Materials science and Engineering Choi, Han Seul; KAIST, Chemistry Choi, Jin; KAIST, Lee, Kug-Seung; Pohang Accelerator Laboratory, Celestre, Richard; Lawrence Berkeley National Lab, Advanced Light Source Shapiro, David; Lawrence Berkeley National Lab, Advanced Light Source Park, Jeong; KAIST, Chemistry Kim, Chunjoong; Chungnam National University, Department of Materials Science and Engineering Yu, Young-Sang; Chungbuk National University Kim, Hyun You; Chungnam National University, Department of Nanomaterials Engineering

SCHOLARONE™
Manuscripts

ARTICLE

Promoting inherent catalytic activity and stability of TiO_2 supported Pt single-atoms at CeO_x-TiO_2 interfaces

Received 00th January 20xx,
Accepted 00th January 20xx

DOI: 10.1039/x0xx00000x

Mi Yoo,‡[a] Eunji Kang,‡[a] Hyuk Choi,‡[a] Hyunwoo Ha,[a] Hanseul Choi,[b,c] Jin-Seok Choi,[d] Kug-Seung Lee,[e] Richard Celestre,[f] David A. Shapiro,[f] Jeong Young Park,*[b,c] Chunjoong Kim,*[a] Young-Sang Yu*[f,g] and Hyun You Kim*[a]

Single-atoms Single-atoms (SAs) with atomically coordinated reaction centers are considered the next generation catalyst that can reveal exceptional catalytic efficiency. However, the general concern about thermodynamic vulnerabilities of the SAs questions their practical values. Moreover, whether the inherent catalytic nature of SA is superior compared with that of the larger nanoparticles is still under debate. Here, we address two controversies by the comparative study using two catalysts: Pt/TiO_2 and Pt/CeO_x-TiO_2. Based on a hierarchical study of density functional theory, time-resolved catalysis performance test, in-situ infrared spectroscopy, and operando X-ray absorption spectroscopy, we could unveil the catalytic nature of Pt-SAs and their stability. By utilizing the heterogeneous interface formed between TiO_2 supporting particles and CeO_x clusters formed on the surface of TiO_2, we preferentially synthesized Pt-SAs pinned at the CeO_x-TiO_2 interfaces on CeO_x-TiO_2 hybrid-oxide supports. The strong electronic coupling between the Pt-SAs and the Ce ions at the CeO_x-TiO_2 interfaces promoted the catalytic activity toward CO oxidation of Pt-SAs and improved the long-term stability under the CO oxidation conditions. The CO oxidation activity of Pt-SAs stabilized at the CeO_x-TiO_2 was improved by 13.5 times at 200 °C compared with the Pt-SAs on TiO_2. The results present how to easily improve the activity and stability of Pt-SAs using simple interface control method. Moreover, we demonstrate that the catalytic activity and the stability of Pt-SAs can be monitored through the chemical sate of the interfaces. Our study delivers comprehensive understating about the catalytic nature as well as a novel strategy toward applications of Pt-SAs, enabling sustainable use of Pt in heterogeneous catalysts.

Introduction

The overall catalytic performance of an oxide supported metal catalyst is an ensemble of activity, selectivity, and stability. Since the high price of metal catalysts that are typically earth-unabundant precious metals hinders the economic usage of the catalysts, one of the primary targets is the design of better performing heterogeneous catalysts. The seminal findings about the high catalytic activity of oxide-embedded metal ions[1, 2] and sub-nanometer-sized metal clusters[3-5] stimulated the catalysis communities to scrutinize the catalytic nature of the smaller metal species with the higher surface-to-volume ratio. The size-dependent catalytic properties of metal nanoparticles (NPs) have been intensively studied. Unraveled catalytic function of the metal-oxide interfaces of which density is an inverse function of the size of metal NPs[6, 7] and the nature of the size-dependent electronic interaction between metal NPs and supporting oxides[8, 9] extended our ability toward rational catalyst design with atomic precision.

The recent pioneering finding reported by Qiao et al., in which Pt single-atoms (SAs) can be stabilized on an oxide support and utilized for catalytic reaction, brought the SA-based catalysts into the framework of conventional catalysis study[10]. The significant research effort about the SA-based catalysts conducted over the last decade proved that SAs assure the enhanced catalytic activity per unit mass of precious metal[7, 10-13]. By utilization of every individual atom as a well-confined reaction site, the SA-based catalysts are considered the ultimate solution for sustainable use of earth unabundant precious metal such as Pt or Au[12].In particular, the atomically confined reaction sites provided by SAs homogenize the reaction pathway, thus improving the selectivity[14, 15].

Intuitively, SAs densely distributed over the surface of oxide supporting materials leads to the maximum active site density[13]. If the reaction sites provided by an individual SA is catalytically more reactive than those of the larger clusters or NPs, the dense SA-based catalyst assures both high economic

[a] Department of Materials Science and Engineering, Chungnam National University, Daejeon 34134, Republic of Korea E-mail: kimhy@cnu.ac.kr, E-mail: ckim0218@cnu.ac.kr
[b] Center for Nanomaterials and Chemical Reactions, Institute for Basic Science (IBS), Daejeon 34141, Republic of Korea E-mail: jeongypark@kaist.ac.kr
[c] Department of Chemistry, Korea Advanced Institute of Science and Technology (KAIST), Daejeon 34141, Republic of Korea
[d] KAIST Analysis Center for Research Advancement, Korea Advanced Institute of Science and Technology (KAIST), Daejeon 34141, Republic of Korea
[e] Pohang Accelerator Laboratory, Pohang University of Science and Technology, Pohang 37673, Republic of Korea
[f] Advanced Light Source, Lawrence Berkeley National Laboratory, Berkeley, California 94720, United States of America
[g] Department of Physics, Chungbuk National University, Cheongju 28644, Republic of Korea E-mail: youngsang@chungbuk.ac.kr

†Electronic Supplementary Information (ESI) available: Detailed experimental and theoretical methods and additional characterization. See DOI: 10.1039/x0xx00000x

‡ These authors contributed equally to this work

efficiency and high activity[13, 16]. However, the general concern about thermodynamic vulnerabilities of the SAs questions their practical application regarding the stability under the reaction conditions[13]. Although SAs comprise good material efficiency owing to their high surface-to-volume ratio, thermodynamic instability of SAs can drive agglomeration of SAs to large clusters or NPs[13, 17].

To synthesize and stabilize dense SAs on a supporting material, specific strong SA binding sites are required, which make SAs stable against thermodynamically driven agglomeration or ripening[17-19]. Recent relevant findings showed that the certain type of structural ensembles can further stabilize the SAs on supporting oxides through delicate balance between the SA-adsorbate and the SA-support interactions[18-23]. For example, Pt-SAs could be stabilized as a form of the planar PtO_4 at the step edges of CeO_2[24]. Li and coworkers directly visualized the disintegration of NPs into SAs led by the strong thermodynamic stability of the local Pd-N_4 ensemble in the metal-organic framework support by *in situ* transmission electron microscopy (TEM)[21]. The consecutive findings reported by the Wang and the Datye groups confirmed that the polyhedral CeO_2 supported Pt-SAs are stable up to 800 °C under the reactive conditions[23, 25, 26]. Covalent bond formation among under-coordinated Ce^{3+} ions, Pt-SAs, and bridging oxygen ions led to the high thermal stability of Pt-SAs under the harsh conditions[26]. The similar finding was reported by Zhang, Li, Qiao and coworkers in the Pt-SA/FeO_x system, where the Pt-SAs could be successfully stabilized by a strong covalent metal-support interaction (CMSI)[27]. Therefore, fine tuning of the support for strong CMSI has attracted great attention as a promising strategy for the synthesis of stable but dense SAs[18, 26, 27].

In addition to the attentions on structural stability of SAs, recent findings highlighted that the local structural and electronic ensemble of SAs are highly correlated with their catalytic activity[28-32]. The recent report by the Christopher group demonstrated that the catalytic activity of TiO_2 supported Pt-SAs is highly dependent to the local Pt-O(OH) coordination environments[29]. Depending on the pretreatment conditions, they observed prominent shifts in infrared spectra of adsorbed CO on Pt-SA[29]. Indeed, utilizing the oxide supported oxide clusters as a catalyst has been one of the classic approaches in heterogeneous catalysis communities[33-38]. As more metal-oxygen ensemble becomes available in SA catalysts, atomic-level precise control of the SA-oxygen ensembles accompanied with the electronic structural change of SAs[29-32] is widening a route toward rational design of SA-based catalysts from the fundamentals[39]. A successful post-modification of the chemical status of the reactive sites in Pt-SA/CeO_2 was reported by Nie et al., by which the catalytic nature of pre-synthesized Pt-SAs can be further optimized toward specific chemical reaction[25].

Besides, catalytic superiority of the inherent catalytic nature between SAs and NPs is still under debate. The report by Stair and coworkers showed that Pt NPs are reactive for both CO oxidation and water-gas shift reaction, whereas Pt-SAs behave as spectators due to the CO poisoning[40]. The Cargnello group recently demonstrated the severe loss of initial activity of Al_2O_3 supported Pd NPs during methane oxidation, which is accounted for the decomposition of Pd NPs into SAs[41]. In addition, Corma and coworkers also reported that several oxide supported Pt-SAs become more reactive upon gradual agglomeration into NPs[42]. The more reactive catalytic working sites toward hydrogenation, dehydrogenation, and oxidation reactions were consistently observed in the Pt/oxide catalysts with the larger Pt species[42]. If SAs are inherently less reactive than the larger clusters of NPs, the highly acclaimed economic efficiency of SAs-based catalysts should be thoroughly assessed again. Since dynamic structural evolutions of the catalysts during the specific reaction such as decomposition of NPs[41] and agglomeration of SAs[43] can also occur in the metal-oxygen ensemble, unraveling inherent catalytic functionality of SAs can guide the direction toward catalyst optimization.

Herein, CO oxidation reaction ($CO + O_2 \rightarrow CO_2$) is scrutinized as a probe reaction. We comparatively study the catalytic activity and stability of Pt-SAs using two different catalyst systems, Pt/TiO_2 and Pt/CeO_x-TiO_2, to provide fundamental understanding about the size-dependent catalytic activity of TiO_2 supported Pt catalysts and confirm the stabilization of Pt-SAs by the CMSI-based Pt-oxide interface confinement. The hierarchical protocol of density functional theory (DFT) calculation, time-resolved catalyst performance test, temperature-resolved diffuse reflectance infrared spectroscopy (DRIFTS) analysis, and *operando* synchrotron-based X-ray absorption spectroscopy (XAS) study enabled us to unveil the catalytic nature and stability of Pt-SAs. Furthermore, we present the record-high specific rate and excellent long-term stability of Pt-SAs confined at the CeO_x-TiO_2 interfaces toward CO oxidation. Our study delivers comprehensive understating about the catalytic nature as well as a novel strategy toward applications of Pt-SA-based catalysts, ultimately leading to the sustainable use of Pt in heterogeneous catalytic reactions.

Results and discussion

Structural analysis of as-synthesized Pt/TiO_2 and Pt/CeO_x-TiO_2 catalysts. We synthesized two types of Pt catalysts supported on conventional TiO_2 oxide powders (hereafter referred to as *n*PT, where *n* indicates the amount of Pt-loading in wt.%) or on CeO_x-TiO_2 hybrid oxide powders (hereafter, *n*PCT). The CeO_x-TiO_2 hybrid oxide support was prepared by deposition of 1 wt.% of Ce ions on the surface of TiO_2 powders (diameter ≈ 25 nm) followed by oxidation, where separated dense CeO_x clusters were uniformly distributed on the surface of TiO_2 powders[18]. The CeO_x-TiO_2 hybrid oxide support with the initial Ce ion content of 1 wt.% supplies dense CeO_x-TiO_2 interfaces that render stabilization of the most supported Pt (0.25 wt.%) as a form of the SA (initial Ce to Pt atomic ratio was set to be 3.4 : 1) through strong Pt-Ce electronic interaction[18]. In addition, few Pt-SAs could be observed even in the higher Pt-loading *n*PCT catalyst (*n* = 1.0 wt.%) as probed by scanning transmission electron microscopy (STEM) and XAS analyses[18]. However, in this study, only *n*PT and *n*PCT catalysts with low Pt-loadings (*n* = 0.05, 0.1, and 0.25 wt.%) were of interest to exclusively study the inherent catalytic properties of oxide supported Pt-SAs and

This journal is © The Royal Society of Chemistry 20xx

Please do not adjust margins

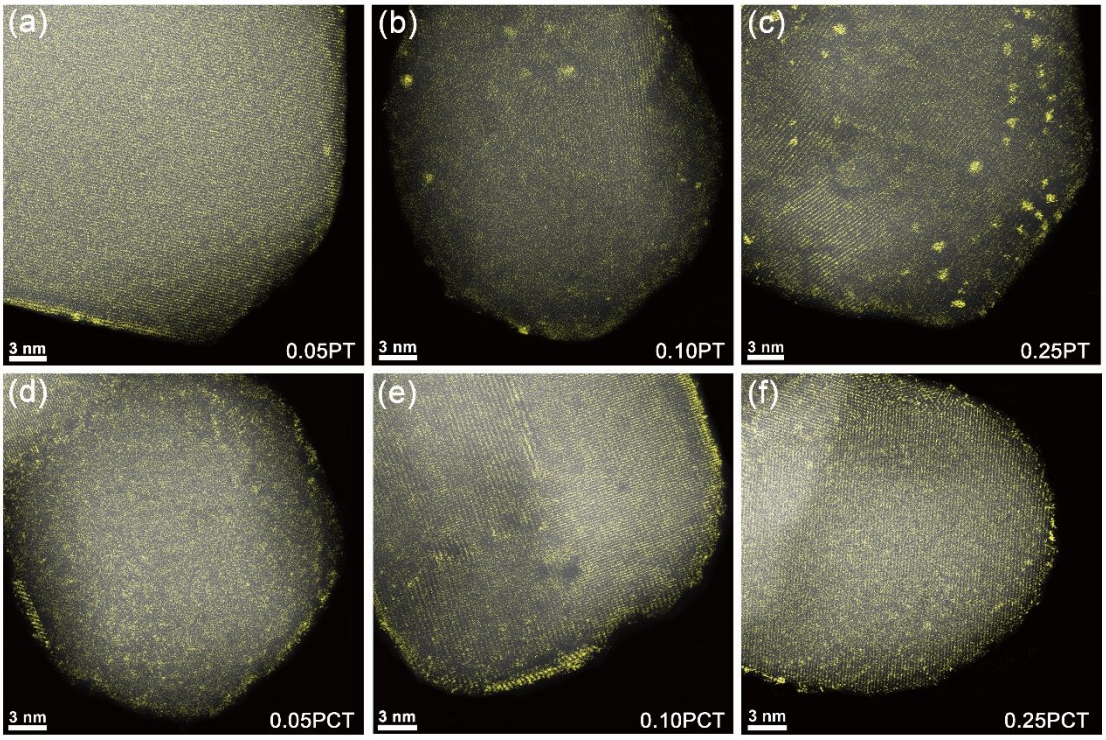

Fig. 1 High-angle annular dark-field (HAADF) STEM images of *n*PT and *n*PCT catalysts with *n* = 0.05, 0.1, and 0.25 wt.%. (a) 0.05PT, (b) 0.10PT, (c) 0.25PT, (d) 0.05PCT, (e) 0.10PCT, and (f) 0.25PCT.

identify the interplay between the interface and the ensemble effects on the catalytic activity and stability of Pt-SAs.

The STEM images of *n*PT and *n*PCT catalysts (*n* = 0.05, 0.1, and 0.25 wt.%) are presented in Fig. 1. The CeO_x-TiO_2 interface drives the preferred generation of Pt-SAs as confirmed in the earlier study[18]. The tiny bright spots that appeared in *n*PCT and 0.05PT catalysts are a distinctive feature of Pt-SAs formed on oxide supports (Fig. 1). While relatively larger Pt clusters with a sub-nanometer size existed in the 0.10PT and 0.25PT systems, such large-sized Pt clusters were not observed in all *n*PCT catalysts, indicating that the CeO_x-TiO_2 interfaces successfully stabilized supplied Pt into Pt-SAs. The deconvoluted X-ray photoelectron spectroscopy (XPS) spectra agreed well with the observation by STEM images. No metallic Pt (Pt^0) was detected in 0.05PT, 0.05PCT, and 0.10PCT catalysts (Fig. S1 and Table S1 in the ESI†), which means that all supplied Pt was atomically dispersed over the surface of TiO_2 (0.05PT) or CeO_x-TiO_2 (0.05PCT and 0.10PCT).

Size dependent catalytic activity in *n*PT: deactivated Pt-SA-TiO_2 interfaces. The temperature-programmed CO conversion profiles (light-off curves) and the corresponding Arrhenius plots of *n*PT catalysts are presented in Fig. 2a, b. Clear size-dependency is observed in the catalytic activities toward CO oxidation. Interestingly, 0.05PT revealed the significant increase in the apparent activation energy barrier for CO oxidation, E_{act}, compared with 0.25PT (E_{act} = 1.22 eV for 0.05PT *vs*. E_{act} = 0.69 eV for 0.25PT). Such increase in E_{act} corroborates that the smaller Pt-species in 0.05PT, Pt-SAs, is less reactive for CO oxidation than the larger Pt-species in 0.25PT, Pt-NPs (Fig. 2a). As a result, the light-off curve of 0.05PT is shifted to the higher temperature region from that of 0.25PT (Fig. 2b). These prominent kinetic data concurrently support that the Pt-SAs supported on TiO_2 are inferior to the larger Pt clusters for CO oxidation. Furthermore, the remarkable increase in E_{act} of 0.05PT suggests that the chemical activity of the Pt-SA-TiO_2 interface toward CO oxidation differs from that of the Pt-NP-TiO_2 interface.

Because the oxygen-release ability of the metal-oxide interface is directly related to the catalytic activity of the interface during oxidation reaction[44-46], we calculated the oxygen vacancy formation energy, E_{vac}, of two different Pt/TiO_2 models, Pt_1/TiO_2 and Pt_9/TiO_2, which closely resemble the Pt-SAs and clusters (or NPs) supported on TiO_2, respectively (Fig. 3a, b). The DFT-calculated E_{vac} of Pt_1/TiO_2 (E_{vac} = 3.65 eV), which is higher than that of Pt_9/TiO_2 (E_{vac} = 2.20 eV), explicitly evidences that the interfacial oxygen of Pt_1/TiO_2 is less reactive. In turn, the higher CO_2 desorption energy of Pt_1/TiO_2 (E_{des} = 2.91 eV) than Pt_9/TiO_2 (E_{des} = 1.28 eV) can explain the trend expected from E_{vac} values. Lastly, the calculated Pt-TiO_2 interaction energy is three times greater in Pt_1/TiO_2 (-2.90 eV/Pt atom) compared with that in Pt_9/TiO_2 (-0.77 eV/Pt atom). All in all, the lattice oxygen ion is strongly bound to the Pt-SA of Pt_1/TiO_2, thus being reluctant to oxidize Pt-CO*. Our experimental and theoretical results on the relative catalytic inferiority of TiO_2 supported Pt-SAs to the larger Pt clusters are consistent with the previous reports which claimed the CO-poisoning vulnerabilities of the Pt-SAs under the CO oxidation conditions[40] and the deactivation of the Al_2O_3 supported Pd NPs upon decomposition into SAs[41]. An inverse relationship between CO oxidation activity and the diameter of ceria supported Pt NPs larger than 1.6 nm was also reported by Cargnello *et al*.[6].The smaller the NPs, the greater the turnover frequency (TOF),

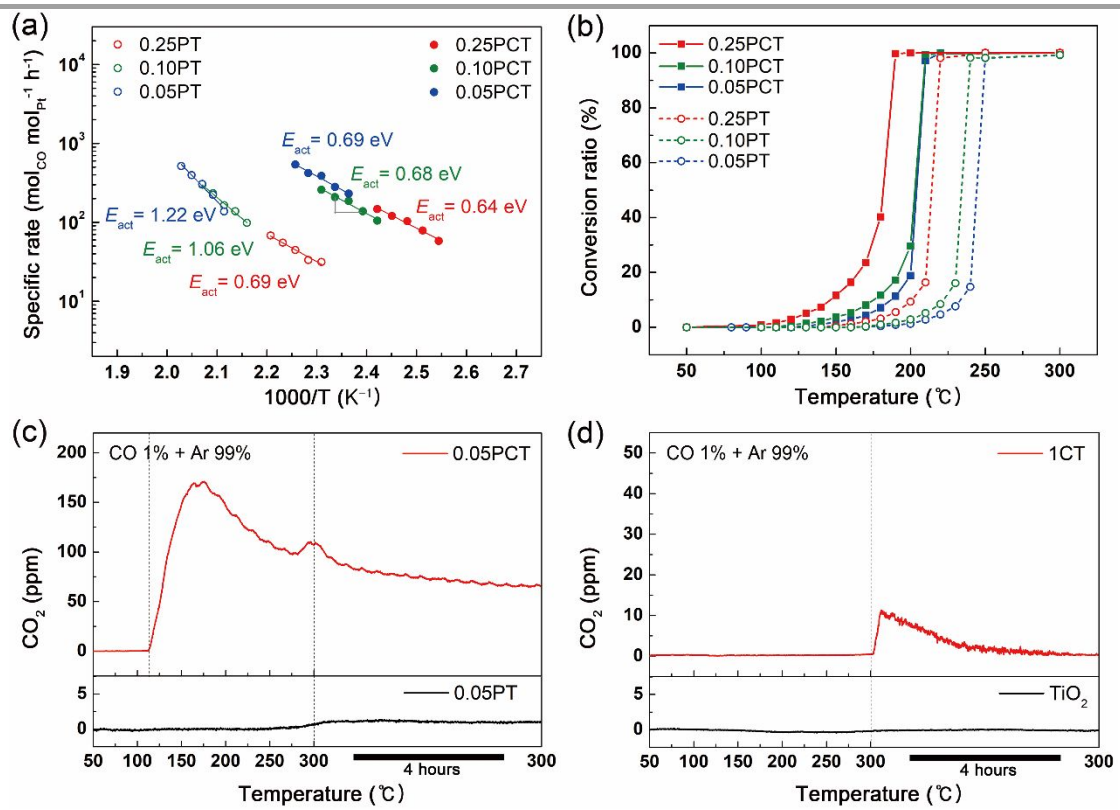

Fig. 2 CO oxidation performance of *n*PT and *n*PCT catalysts. (**a**) Pt size dependent apparent activation energy barrier, E_{act}, of *n*PT and *n*PCT catalysts. The *n*PCT catalysts in which the CeO_x-TiO_2 interfaces create the well distributed Pt-SAs show the similar E_{act} values. However, the E_{act} of *n*PT catalysts is significantly increased upon formation of Pt-SAs on TiO_2 (0.05PT). (**b**) Temperature-programmed CO conversion profile (light-off curve) of *n*PT and *n*PCT catalysts. (**c**) CO-TPR analysis results of 0.05PCT and 0.05PT. (**d**) CO-TPR analysis results of CeO_x-TiO_2 and TiO_2 support powders.

which is attributed to the higher density of the interfacial Pt atoms that work as reaction centers in the smaller NPs[6]. Contrary to the general consensus that SAs with the maximized metal-oxide interface density deliver high activity and improved material efficiency, especially for the interface-mediate catalytic reaction[12, 13], our results predict that the decrease in the activity at the interfaces between Pt-SAs and TiO_2 deteriorates the catalytic performance of TiO_2 supported Pt-SAs. Because the inherent catalytic activity of the Pt-TiO_2 interface of 0.05PT is lower than that of 0.25PT, we hypothesize that there would be a critical Pt cluster size at which the mass normalized specific catalytic activity of Pt reaches the maximum. However, the CO oxidation activity of TiO_2 supported Pt-SAs was optimized by pretreatment[29] and the steam-treated Pt-SAs on CeO_2 exhibited the enhanced low-temperature activity toward CO oxidation[25]. Therefore, we note that our finding on the relative catalytic inferiority of Pt-SAs in 0.05PT compared with Pt-NPs in 0.25PT should not be overrated as a general principle. Depending on the reaction, the relative catalytic superiority between Pt-SAs and Pt-NPs supported on TiO_2 could be reversed.

Catalytic promotion of Pt-SAs at CeO_x-TiO_2 interfaces. On the contrary, the consistent E_{act} values were obtained over three *n*PCT catalysts (Fig. 2a). This implies that the *n*PCT catalysts supply the same kind of major reaction site for CO oxidation albeit with different Pt-loading. Because of the relatively lower E_{act} values of *n*PCT than those of *n*PT (Fig. 2a), the *n*PCT catalysts completed the CO oxidation at the lower reaction temperature (Fig. 2b). Based on the STEM images (Fig. 1d-f) and the kinetic data (Fig. 2a, b), it is strongly believed that the same kind of Pt-SAs stabilized at the CeO_x-TiO_2 interfaces but with different Pt-SA densities were formed over three *n*PCT catalysts. Our finding confirms that intensive density control of Pt-SAs is available at the CeO_x-TiO_2 interface. The XPS spectra shows the appearance of Pt^0 when Pt loading reaches 0.25 wt.%, i.e. 0.25PCT (Fig. S1 and Table S1 in the ESI†), suggesting that 0.25 wt.% is the upper-limit of Pt-loading for preferential formation of Pt-SAs on CeO_x-TiO_2 hybrid oxide supports. Additional CO temperature programmed reaction (CO-TPR) analysis were conducted on 0.05PCT with a mixture gas (1 vol.% of CO and 99 vol.% of Ar). The usage of testing gas without oxygen can identify the mechanism as confirmed in our previous study[18]. CO-TPR confirmed that the Pt-CeO_x-TiO_2 interfaces of 0.05PCT vigorously supplied oxygen for CO oxidation at above 110 °C, convincing operation of the interface-mediated Mars-van Krevelen (MvK) mechanism (Fig. 2c). The DFT-calculated schematic diagram of the MvK type CO oxidation pathway catalyzed by a Pt/CeO_x-TiO_2 model is presented in Fig. S2 in the ESI†. Considering the lower E_{vac} in the Pt-SA/CeO_x-TiO_2 model catalyst (2.25 eV) than that of Pt_1/TiO_2 (3.65 eV) (Fig. 3a, c), the interfacial oxygen in 0.05PCT is more reactive. On the other hand, the Pt-TiO_2 interface in 0.05PT was completely inactive even up to 200 °C and little amount of CO_2 was produced at above 250 °C (Fig. 2c). Interestingly, the rapid CO_2 production and quick fading out in the CO-TPR profile of CeO_x-TiO_2 support powders (without Pt, Fig. 2d) support that

This journal is © The Royal Society of Chemistry 20xx

Please do not adjust margins

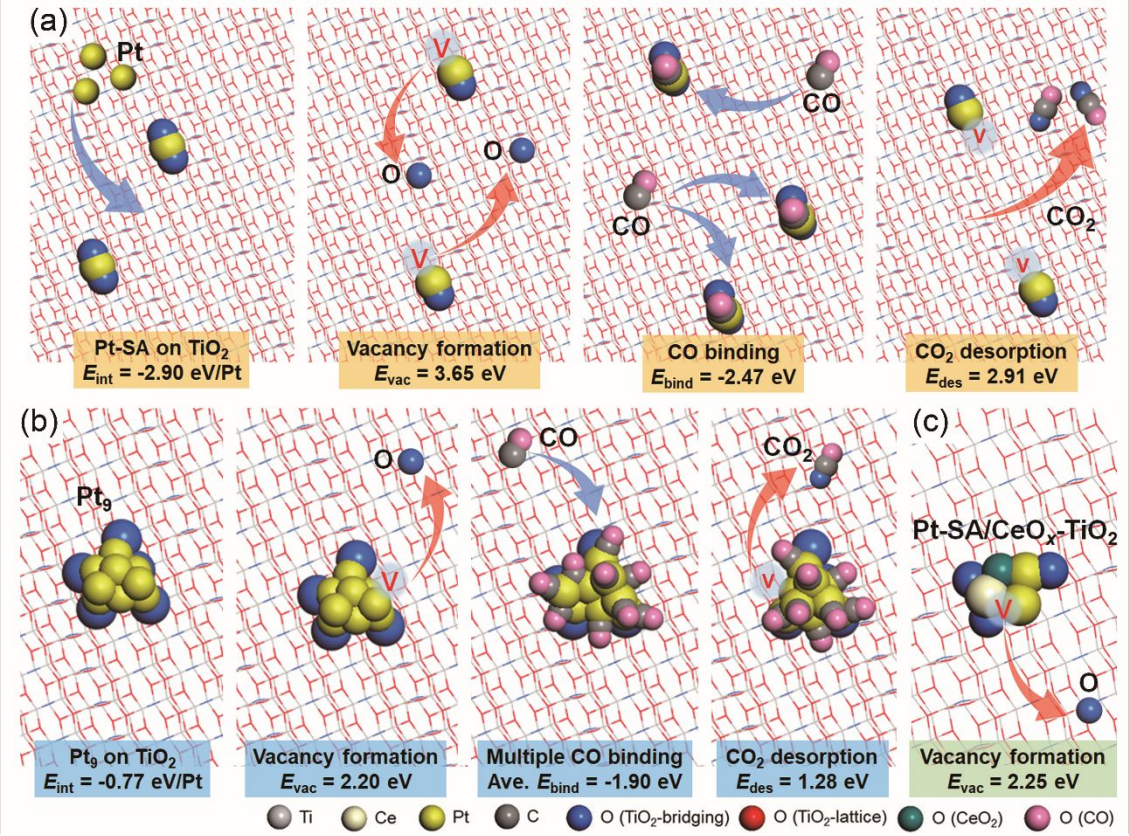

Fig. 3 Long-term CO DFT-estimated interface chemistry of Pt catalysts. (a) Pt-SA on TiO_2, (b) Pt_9 on TiO_2, and (c) Pt-SA on CeO_x-TiO_2. The E_{int} denotes the normalized Pt-TiO_2 interaction energy. The E_{vac} and E_{des} corresponds to the energy of oxygen vacancy formation and the energy of CO_2 desorption (production), respectively. The E_{bind} is the energy of CO binding on Pt. The averaged E_{bind} of total 9 CO molecules is presented in (b).

the CeO_x-TiO_2 interfaces work as the structurally and chemically well-regulated homogeneous oxygen supply sites. Whereas, CO_2 production was not observed in TiO_2 powders (Fig. 2d). Because CeO_x alone does not strongly bind CO[47], the continuous CO_2 production tail in 0.05PCT during constant temperature CO-TPR performed at 300 °C (Fig. 2c) indicates that the Pt-CeO_x-TiO_2 interface is the oxygen supply gateway for oxidation of Pt-CO*. The Pt-CeO_x-TiO_2 interfaces trigger continuous oxygen supply from TiO_2 under the CO-TPR conditions (refer to Fig. 2c and 2d). The consistent positive order of reaction values with CO of 0.05PCT (0.39) and 0.25PCT (0.34) show that the reaction sites in 0.05PCT and 0.25PCT are catalytically identical and resistant to CO-poisoning (Fig. S3a, b in the ESI†). On the other hand, the highly negative order of reaction found in 0.05PT (-0.67) confirm that the Pt-SAs in 0.05PT are strongly CO-poisoned (Fig. S3c, d in the ESI†). The theoretical rate map (Fig. S4 in the ESI†) was derived by microkinetic modeling based on DFT-calculated energetics of the MvK type of CO oxidation. The rate map demonstrated that Pt-SAs at the CeO_x-TiO_2 interfaces facilitate CO oxidation at above 100 °C. The rapid increase in the reaction rate at around 200 °C reproduces the experimental behavior of 0.05PCT presented in the light-off profile (Fig. 2b).

The site normalized reaction rate *vs*. reaction temperature profile of 0.05PT showed that the overall reaction temperature was retarded to the higher temperature from that of 0.05PCT due to the higher E_{act} of 0.05PT (Fig. S5 in the ESI†). The inherent catalytic activity of 0.05PCT is 13.5 times greater than that of 0.05PT at 200 °C, corroborating the excellent activating power of the CeO_x-TiO_2 interfaces. The excellent promotional effect of the Pt-CeO_x-TiO_2 interfaces boosts the specific CO oxidation rate of 0.05PCT and 0.10PCT, therefore the TOF of 0.05PCT prevail most of the literature-available data points (Table S3 in the ESI†). However, it should be noted that the TOF can be highly influenced by the catalyst test conditions such as space velocity, reactant concentration, and temperature at which TOF is estimated.

Along with recent findings about atomic-precision optimization of the interfaces between metal SAs and oxide supporting materials followed by the enhancement in both catalytic activity and stability of SAs[23-27, 29-32, 48-50], our findings about *n*PCT catalysts also demonstrate that the specific Pt-CeO_x-TiO_2 interface ensemble regulates the reaction pathway and activates Pt-SAs. The chemical accessibility of the interfacial oxygen ions at the vicinity of Pt-SAs can be controlled by pre- or post- treatment processes[25, 29], therefore the catalytic performance of 0.05PCT can be further improved through the optimization of Pt-CeO_x-TiO_2 interfaces. The relatively reactive oxygen species with the lower E_{vac} in CeO_x chains or plates[51] can lower the light-off temperature of Pt-SAs.

Because the binding energy, E_{bind}, of a Pt-SA on a pristine TiO_2(101) surface (-2.94 eV) is weaker than that at the CeO_x-TiO_2 interface (-4.02 eV)[18], the energy for Pt abstraction from the CeO_x-TiO_2 interface is higher than that from the TiO_2 (101) (Fig. S6 in the ESI†). Therefore, the CeO_x-TiO_2 interface clearly provides an extra stabilization site for Pt-SAs. However, such stabilization of could be achieved owing to the strong structural

and electronic interaction among Pt, Ce, Ti, and O. Different kind of interface combinations should be required to stabilize Au, Pd, or Rh SAs. In addition, it should be noted that Pt-SAs also can be further stabilized in other interfaces.

Improved long-term stability of Pt-SAs at CeO_x-TiO_2 interfaces. In order to investigate the stability of catalyst systems, the prolonged reaction test of the 0.05PCT catalyst was carried out under the exposure to the harsh reaction condition (1 vol.% CO + 4 vol.% O_2 + 95 vol.% Ar at 300 °C) for up to 24 hours (Fig. 4a, refer to Fig. S7 in the ESI† and discussion therein for detailed test process). The E_{act} values of 0.05PCT were preserved even after high-temperature and long-term operation. The negligible change in the activation energy barrier is closely related to the structural and catalytic nature of the key reaction site, i.e. the Pt-CeO_x-TiO_2 interface, which reveals thermodynamic stability even under the harsh reaction environment. Since the physical as well as chemical interactions between Pt-SAs and CeO_x-TiO_2 interfaces were kept unchanged during the reaction condition, Pt-SAs of as-synthesized 0.05PCT, 0.05PCT-As, were not agglomerated into the larger clusters or NPs but stabilized as the initial structure of the SA. On the other hand, the 0.05PT-As catalyst exposed to the same reaction condition showed significant decrease in E_{act} from 1.23 eV to 0.74 eV, even after shorter oxidation of CO (12 hours). It is elucidated that the catalytic nature of the Pt-TiO_2 interface could not be preserved during the long-term CO oxidation test (Fig. 4b). Note that the lowest E_{act} value among the *n*PT catalysts was observed in 0.10PT with the largest Pt species (Fig. 2a). The STEM analysis about 0.05PCT (Fig. 4c, 0.05PCT-12h) and 0.05PT (Fig. 4d, 0.05PT-12h) after 12 hours of CO oxidation tests could directly chase the physical change of the Pt-SAs. As expected from the kinetic reaction performance, noticeable agglomerations of Pt-SAs into the larger species were not observed in 0.05PCT-12h. However, the agglomeration of Pt-SAs to NPs was clearly visualized in 0.05PT-12h, which ultimately leads to the decrease in E_{act} (Fig. 4b). The DFT-calculated energy barriers of Pt-SAs diffusing out from the stable binding site on the TiO_2(101) and from the CeO_x-TiO_2 interface (Fig. S6 in the ESI†), confirm the enhanced stability of Pt-SAs of 0.05PCT.

The Pt-L_3 edge X-ray absorption near edge structure (XANES) of 0.05PT-As, 0.05PCT-As, 0.05PCT-24h, and 0.05PT-24h and the corresponding XANES fitting results are presented in Fig. 5a and Table S2 in the ESI†, respectively. The XANES analysis results clearly corroborate that pristine Pt-SAs in 0.05PT-As and 0.05PCT-As show the different mechanistic behavior during the long-term reaction. The significant increase of the metallic Pt in 0.05PT-24h upon long-term reaction supports that the Pt-SAs in 0.05PT-As were agglomerated into Pt clusters or nanoparticles. However, Pt agglomeration was not observed in 0.05PCT-24h, ensuring the excellent long-term stability of Pt-SAs at the CeO_x-TiO_2 interfaces.

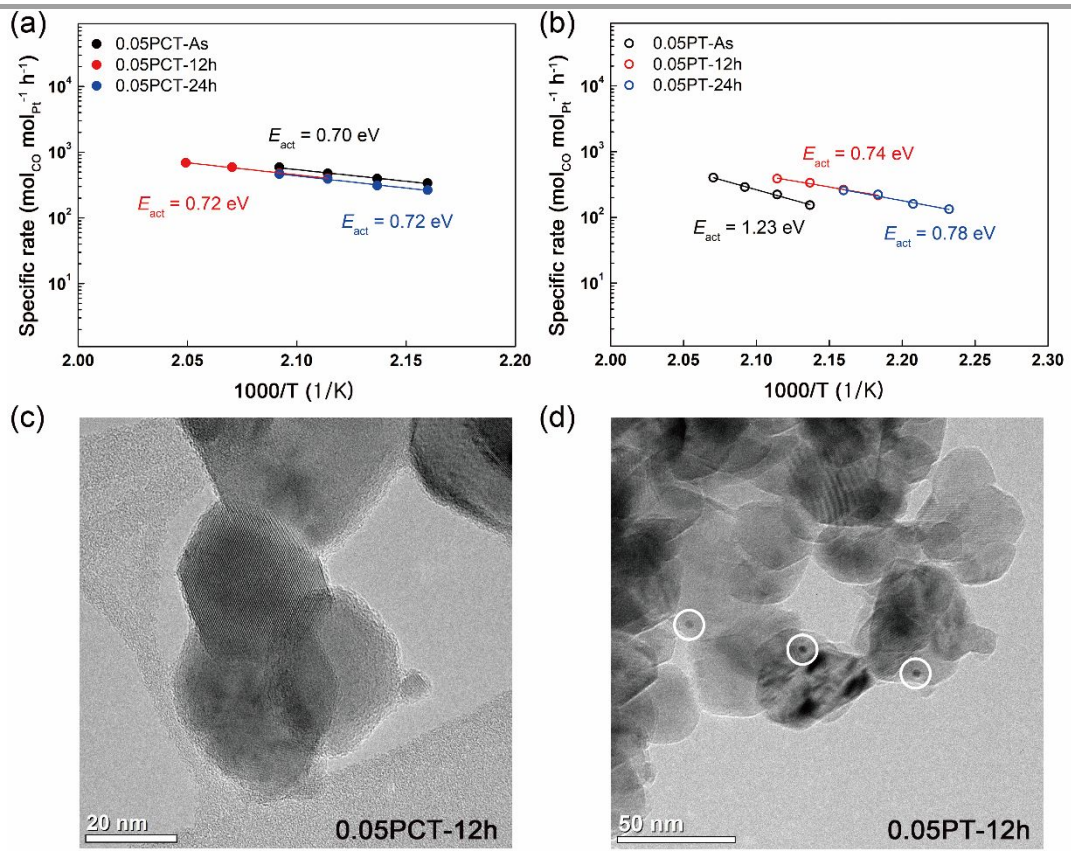

Fig. 4 Long-term CO oxidation test results. The E_{act} of (a) 0.05PCT and (b) 0.05PT catalysts measured before and after the long-term high temperature reaction tests (1 vol.% CO + 4 vol.% O_2 + 95 vol.% Ar at 300 °C). STEM images of (c) 0.05PCT and (d) 0.05PT catalysts after 12 hours of CO oxidation. White circles in (d) represent Pt NPs (diameter ≈ 3 nm). Refer to Fig. S7 in the ESI† and discussion therein for detailed experimental procedure and additional STEM images.

This journal is © The Royal Society of Chemistry 20xx

Please do not adjust margins

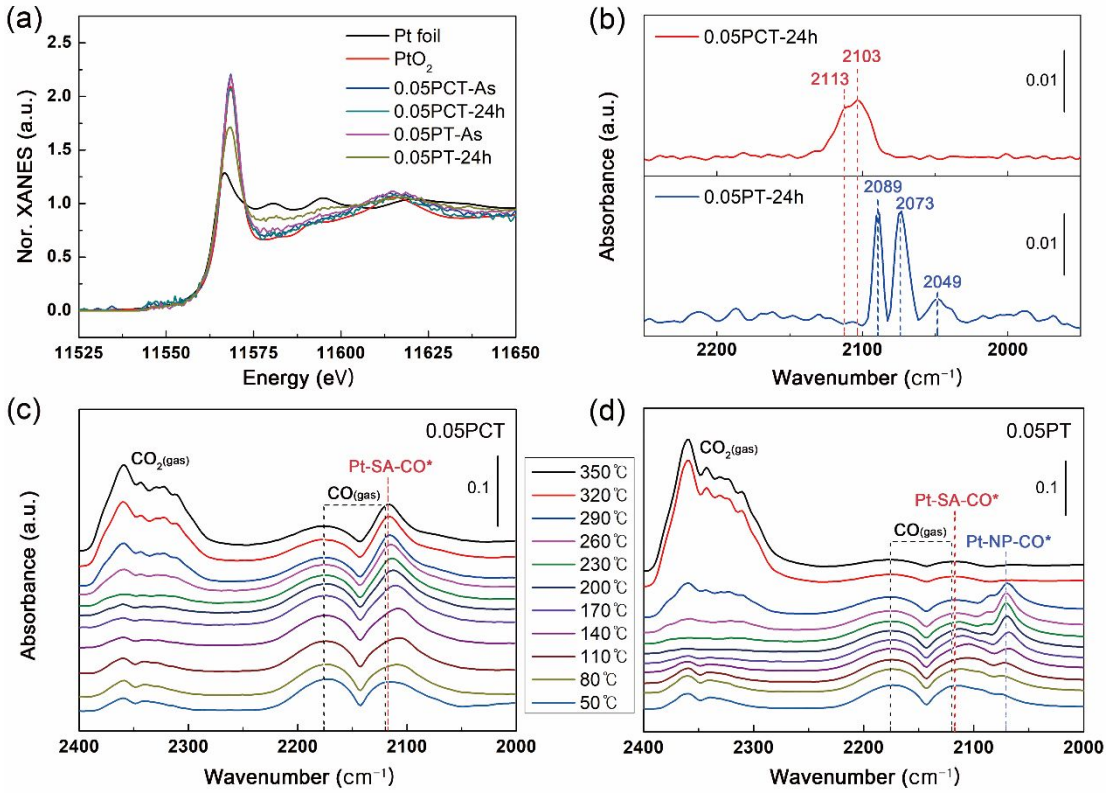

Fig. 5 Spectroscopic evidence of the long-term stability of Pt-SAs in 0.05PCT. (a) Pt-L_3 edge XANES of as-synthesized 0.05PT and 0.05PCT and used 0.05PCT and 0.05PT for 24 hours of CO oxidation test. (b) DRIFTS spectra of used 0.05PT and 0.05PCT catalysts for long-term CO oxidation reaction. (c) Temperature-resolved *in situ* DRIFTS spectra of 0.05PCT. (d) Temperature-resolved *in situ* DRIFTS spectra of 0.05PT.

Fig. 5b shows the DRIFTS spectra of 0.05PCT-24h and 0.05PT-24h. Indeed, the DRIFTS spectra clearly cross-confirmed the core findings of our study that Pt-SAs in 0.05PCT are stable under the reaction conditions. The exclusively observed CO-stretch peaks at 2103 and 2113 cm^{-1} in 0.05PCT-24h confirm that CO molecules were adsorbed on top of Pt-SAs (Pt-SA-CO*)[25, 29, 31, 52]. On the other hand, the red-shifted major peaks at 2089, 2073, and 2049 cm^{-1} in 0.05PT-24h indicate that Pt-SAs in 0.05PT-As were agglomerated into clusters and particles during 24 hours of continuous reaction (Pt-NP-CO*)[26, 52]. Moreover, the temperature-resolved *in situ* DRIFTS spectra of 0.05PCT (Fig. 5c) show the emphasized Pt-SA-CO* peaks which are surviving up to high temperature. On the other hand, new Pt-NP-CO* peaks were emerged upon temperature increase in 0.05PT (Fig. 5d), suggesting that the Pt-SAs in 0.05PT are readily agglomerated into clusters or nanoparticles even at 80 °C due to their instability.

Time-resolved *operando* XAS analysis of long-term stability of Pt-SAs. Among the cutting-edge analysis methods, synchrotron-based *operando* X-ray spectromicroscopy has recently applied for the direct observation about noble metal SA catalysts[11, 53]. The intimate physical and chemical contacts between Pt-SAs and CeO_x-TiO_2 interfaces enable an in-depth analysis about the stability of Pt-SAs with time-resolved *operando* XAS monitoring of Ce ions. A schematic diagram shown in Fig. 6a, b presents how the Ce^{4+} (or the Ce^{3+} *vice versa*) concentration in a *n*PCT catalyst responses to the structural evolution of Pt-SAs (Adapted by permission of The Royal Society of Chemistry)[18]. The synchrotron-based scanning transmission soft X-ray microscopy (STXM) combined with a liquid-flowing nanoreactor could trace spatiotemporally resolved chemical evolution of the Ce ions under the reaction with Pt-precursor solution. The detailed experimental conditions are available in our previous report[18]. As Pt-SAs are being formed at the CeO_x-TiO_2 interfaces, they donate electrons to adjacent Ce ions, resulting in the decrease in the Ce^{4+} concentration of the CeO_x-TiO_2 interface (from stage 1 to 3, Fig. 6b). However, once all available CeO_x-TiO_2 interfaces are occupied by Pt-SAs, newly introduced Pt ions are agglomerated to Pt clusters (stage 4, Fig. 6b). In this stage, the amount of the electron donated from Pt ions to Ce ions decreases, and finally the Ce^{4+} concentration was recovered close to the initial value. Therefore, the *operando* STXM observation provides the spatiotemporal information of Ce ions that can be applied for tracking the structural evolution of Pt-SAs under the catalytic reaction conditions and consequently the long-term structural stability of Pt-SAs[18].

To monitor the potential physicochemical evolution of Pt-SAs of 0.05PCT at the elevated temperature, we performed the *operando* STXM analysis (Refer to Methods and Fig. S8 in the ESI† for more details) about the 0.05PCT catalyst under the inert reaction environment, 100 vol.% Ar flow at 300 °C for 14 hours. The temperature- and time-dependent overall compositions measured over the separated three sample regions consistently proved that the Ce^{4+} concentration of 0.05PCT did not significantly change during the long-term exposure to Ar at 300 °C (Fig. S9 in the ESI†). Considering that 0.05PCT catalyst completely convert the supplied CO to CO_2 at above 200 °C (T_{100}), the negligible change of Ce^{4+} at the environmental

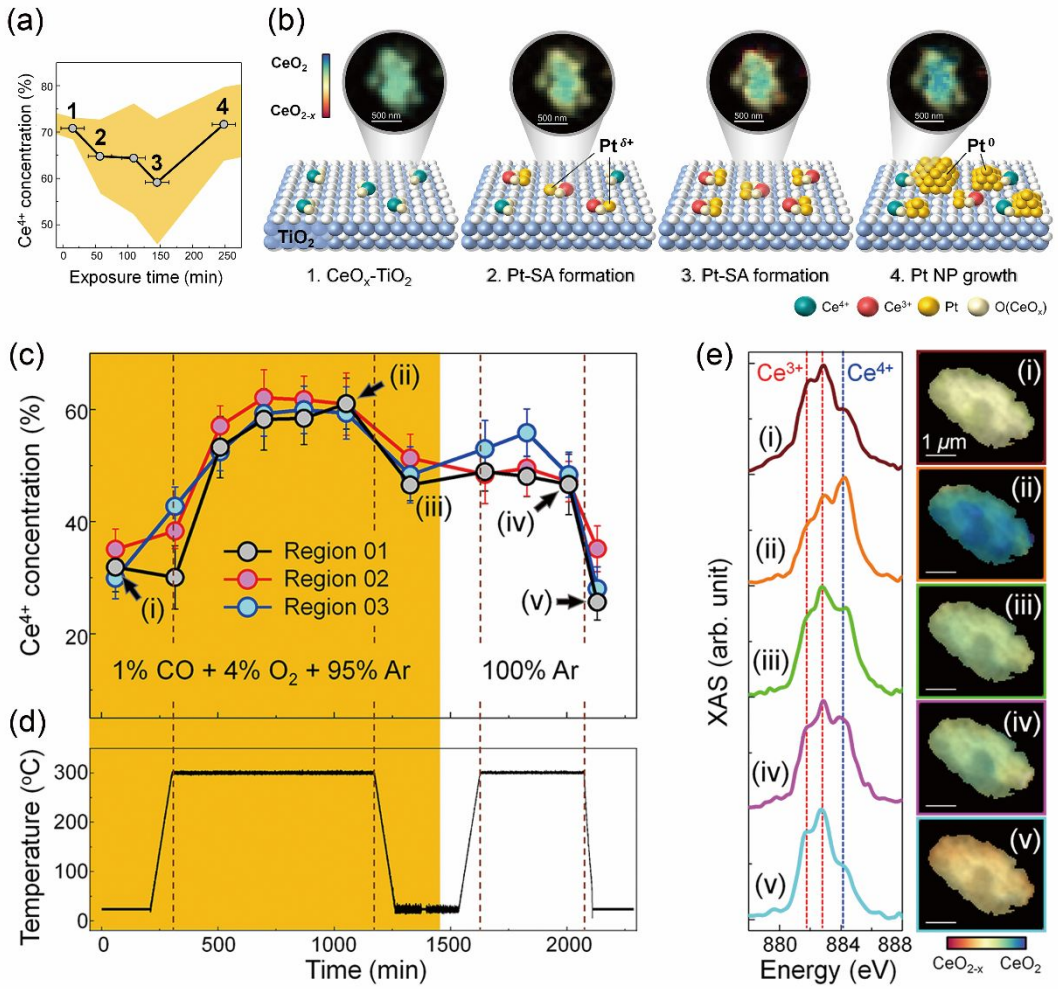

Fig. 6 Spatiotemporally resolved chemical evolutions of *n*PCT catalyst system. (**a** and **b**) Schematic diagram showing the correlation between the Pt-size and the Ce^{4+} concentration in *n*PCT catalyst system. The original *operando* liquid STXM results are adapted from our previous report (Adapted by permission of The Royal Society of Chemistry)[18]. (**a**) Ce^{4+} concentration measured *versus* exposure time. The time-dependent Ce^{4+} concentration of the CeO_x-TiO_2 particles with 6 wt.% of initial Ce-loading is plotted as a function of the exposure time to a circulating solution containing Pt-precursors. The numbered data points in (**a**) represent the averaged Ce^{4+} concentration over the measured areas. The yellow shaded area indicates the standard deviation. (**b**) Schematic Pt-SA or cluster models corresponding to the *operando* STXM data points in (**a**). The increasing areal fraction of the yellowish or reddish region indicates the increasing Ce^{3+}/decreasing Ce^{4+} concentrations upon Pt-SAs formations (from stage 1 to stage 3). The original Ce^{4+} concentration is recovered as Pt clusters are appeared (stage 4). (**c**-**e**) *Operando* Ce chemical maps of 0.05PCT in real CO oxidation condition (1 vol.% CO + 4 vol.% O_2 + 95 vol.% Ar at 300 °C, orange shaded area) and following temperature elevation with 100 vol.% Ar flowing (up to 300 °C, white shaded area). (**c** and **d**) Averaged Ce^{4+} concentrations from three sample regions with respect to the temperature profile. The error bars in (**c**) indicate the standard deviation. Chemical information was obtained by linear combination fits of XAS data with reference spectra (Fig. S10 in the ESI†) (**e**) *Operando* XAS from the region 1 (left) and their spatiotemporal chemical evolutions (right) specified in (**c**). Energy positions of M_5-edge absorption features for Ce^{3+} and Ce^{4+} are indicated as dotted red and blue lines, respectively. The fitting results (chemical information) and averaged optical density (morphological information) at each pixel were presented by color legend and transparency, respectively. The presence of CeO_2 and CeO_{2-x} assigned colors blue and red, respectively.

condition of the nanoreactor corroborates the excellent structural stability of the Pt-SAs at the CeO_x-TiO_2 interfaces even at high temperature. Moreover, the electronic state of the Pt-CeO_x-TiO_2 interface, which critically contribute to the chemical activity of the interface, was well preserved during the measurement, again highlighting the high catalytic consistency of our 0.05PCT catalyst.

Based on the long-term physical and chemical stability of Pt-SAs in 0.05PCT under the inert Ar atmosphere at 300 °C, we exposed the 0.05PCT catalyst to the real CO oxidation condition (1 vol.% CO + 4 vol.% O_2 + 95 vol.% Ar at 300 °C). Interestingly, the *operando* STXM analysis observation (Fig. 6c-e and Fig. S11 in the ESI†) showed the rapidly increasing Ce^{4+} concentration over the exposure time. If Pt-SAs of 0.05PCT are clustered during the high-temperature CO oxidation reaction, the larger Pt clusters do not donate as much electrons as Pt-SAs do to adjacent Ce ions (Fig. 6b), in turn leading to the increase of the Ce^{4+} concentration. However, after cooling down to the room-temperature followed by 4 hours of additional stabilization and subsequent 5 hours of high-temperature Ar-treatment processes at 300 °C, the Ce^{4+} concentration of 0.05PCT was decreased again and completely recovered to the initial value. Because the 0.05PCT catalyst did not show any notable change in the Ce^{4+} concentration during the long-term heat treatment under the 100 vol.% Ar condition (Fig. S9 in the ESI†), we are convinced that the decreasing Ce^{4+} concentration observed during the second stage heat treatment with pure Ar in Fig. 6c, d was not originated from the structural evolution of Pt-SAs. Rather, because the 0.05PCT catalyst was exposed to the oxygen rich reaction condition (CO : O_2 = 1 : 4) during the long-

This journal is © The Royal Society of Chemistry 20xx

Please do not adjust margins

term reaction test, excess oxygen molecules can be adsorbed on the reduced Ce^{3+} ions and oxidize them to Ce^{4+} ions. In addition, the similar trends in the control groups of which dose damage was minimized confirmed that the beam-induced damage on the sample[54] was negligible (Fig. S12 in the ESI†).

In our previous *operando* gas phase XAS analysis performed on 0.25PCT, we exposed the catalyst to the stream of 7 vol.% CO + 93 vol.% Ar and elevated the reaction temperature from the room temperature to 160 °C[18]. The result showed that the Ce^{4+}/Ce^{3+} ratio was gradually decreased upon exposure to CO as the result of oxygen vacancy formation[18, 44, 45], indicating the operation of the MvK type CO oxidation at the Pt-CeO_x-TiO_2 interfaces. The original Ce^{4+}/Ce^{3+} ratio was recovered as the catalyst was cooled down and exposed to air[18]. Meantime, our current finding that the Ce^{4+}/Ce^{3+} was increasing during the high temperature CO oxidation predicts that the oxygen vacancies at the Pt-CeO_x-TiO_2 interfaces, which are generally formed upon CO_2 production, were rapidly healed by O_2 under the oxygen rich reaction condition. The continuously decreasing Ce^{4+} concentration observed during the second heat treatment stage in Fig. 6c confirms that these chemisorbed oxygen molecules were gradually desorbing. The control group samples exhibited the same trend confirming the reliability of the data points. Our *operando* gas XAS analysis results corroborate the excellent physicochemical stability of Pt-SAs at the CeO_x-TiO_2 interfaces.

Conclusions

Herein, our experimental and theoretical findings evidence the catalytic superiority of the Pt-SAs at the CeO_x-TiO_2 interfaces in both catalytic activity and long-term stability. We found that the Pt-SAs in 0.05PT were easily CO-poisoned and agglomerated into the larger clusters during CO oxidation reaction. On the other hand, the CeO_x-TiO_2 interface confined Pt-SAs in 0.05PCT facilitated the MvK mechanism during CO oxidation by utilization of the oxygen at the Pt-CeO_x-TiO_2 interface, exhibiting the high specific rate. The time-resolved long-term stability test, the *in situ* DRIFTS, and the *operando* STXM analysis results concurrently confirmed the excellent physicochemical stability of the Pt-SAs at the CeO_x-TiO_2 interfaces. The combined high catalytic activity and stability of Pt-SAs brought together by the CeO_x-TiO_2 interfaces enable extensive design of Pt-SA-based catalysts optimized for the given chemical reactions through fine-tuning of catalytic function of the interfaces. Moreover, the most efficient catalyst support, CeO_x-TiO_2, is provided, which can ensure the highest catalytic activity and the stability of SAs.

Conflicts of interest

There are no conflicts to declare.

Acknowledgements

This work was supported by the National Research Foundation of Korea (NRF) grant funded by the Korean government (Ministry of Science, ICT and Future Planning, MSIP) (2019R1A2C1089256). C.K and H.Y.K thank to the support from the Basic Science Research Program through the NRF funded by the Ministry of Education (2021R1A6A1A03043682). C.K. (2017M3D1A1039561) and K.-S.L (2019M3D1A1079309) thank to the support from the Creative Materials Discovery Program through the NRF funded by the MSIP. Work of H. C. and J. Y. P. was supported by Institute of Basic Science (IBS) [IBS-R004]. This research used resources of the Center for Functional Nanomaterials, which is a U.S. DOE Office of Science Facility, and the Scientific Data and Computing Center, a component of the Computational Science Initiative, at Brookhaven National Laboratory under Contract No. DE-SC0012704. Computing time was also provided by the National Institute of Supercomputing and Network/Korea Institute of Science and Technology Information (KSC-2020-CRE-0259). Work of D.A.S and Y.-S.Y. was supported by the Director, Office of Science, Office of Basic Energy Sciences, of the US Department of Energy (Contract no. DE-AC02-05CH11231). This research used resources of the Advanced Light Source, which is a DOE Office of Science User Facility under contract no. DEAC02-05CH11231.

Notes and references

1. Q. Fu, H. Saltsburg and M. Flytzani-Stephanopoulos, *Science*, 2003, **301**, 935-938.
2. E. W. McFarland and H. Metiu, *Chem. Rev.*, 2013, **113**, 4391-4427.
3. A. A. Herzing, C. J. Kiely, A. F. Carley, P. Landon and G. J. Hutchings, *Science*, 2008, **321**, 1331-1335.
4. J. Oliver-Meseguer, J. R. Cabrero-Antonino, I. Domínguez, A. Leyva-Pérez and A. Corma, *Science*, 2012, **338**, 1452-1455.
5. S. Vajda, M. J. Pellin, J. P. Greeley, C. L. Marshall, L. A. Curtiss, G. A. Ballentine, J. W. Elam, S. Catillon-Mucherie, P. C. Redfern, F. Mehmood and P. Zapol, *Nat. Mater.*, 2009, **8**, 213-216.
6. M. Cargnello, V. V. T. Doan-Nguyen, T. R. Gordon, R. E. Diaz, E. A. Stach, R. J. Gorte, P. Fornasiero and C. B. Murray, *Science*, 2013, **341**, 771-773.
7. L. Liu and A. Corma, *Chem. Rev.*, 2018, **118**, 4981-5079.
8. W. E. Kaden, T. Wu, W. A. Kunkel and S. L. Anderson, *Science*, 2009, **326**, 826-829.
9. Y. Lykhach, S. M. Kozlov, T. Skála, A. Tovt, V. Stetsovych, N. Tsud, F. Dvořák, V. Johánek, A. Neitzel, J. Mysliveček, S. Fabris, V. Matolín, K. M. Neyman and J. Libuda, *Nat. Mater.*, 2016, **15**, 284-288.
10. B. Qiao, A. Wang, X. Yang, L. F. Allard, Z. Jiang, Y. Cui, J. Liu, J. Li and T. Zhang, *Nat. Chem.*, 2011, **3**, 634-641.
11. J. Liu, *ACS Catal.*, 2017, **7**, 34-59.
12. A. Wang, J. Li and T. Zhang, *Nat. Rev. Chem.*, 2018, **2**, 65-81.
13. X.-F. Yang, A. Wang, B. Qiao, J. Li, J. Liu and T. Zhang, *Acc. Chem. Res.*, 2013, **46**, 1740-1748.
14. J. Shan, M. Li, L. F. Allard, S. Lee and M. Flytzani-Stephanopoulos, *Nature*, 2017, **551**, 605.
15. L. Lin, S. Yao, R. Gao, X. Liang, Q. Yu, Y. Deng, J. Liu, M. Peng, Z. Jiang, S. Li, Y.-W. Li, X.-D. Wen, W. Zhou and D. Ma, *Nat. Nanotechnol.*, 2019, **14**, 354-361.
16. A. Beniya and S. Higashi, *Nat. Catal.*, 2019, **2**, 590-602.
17. T. W. Hansen, A. T. DeLaRiva, S. R. Challa and A. K. Datye, *Accounts Chem. Res.*, 2013, **46**, 1720-1730.
18. M. Yoo, Y.-S. Yu, H. Ha, S. Lee, J.-S. Choi, S. Oh, E. Kang, H. Choi, H. An, K.-S. Lee, J. Y. Park, R. Celestre, M. A. Marcus, K. Nowrouzi, D. Taube, D. A. Shapiro, W. Jung, C. Kim and H. Y. Kim, *Energy Environ. Sci.*, 2020, **13**, 1231-1239.

19. J.-C. Liu, Y.-G. Wang and J. Li, *J. Am. Chem. Soc.*, 2017, **139**, 6190-6199.
20. Y. G. Wang, D. Mei, V. A. Glezakou, J. Li and R. Rousseau, *Nat. Commun.*, 2015, **6**, 6511.
21. S. Wei, A. Li, J. C. Liu, Z. Li, W. Chen, Y. Gong, Q. Zhang, W. C. Cheong, Y. Wang, L. Zheng, H. Xiao, C. Chen, D. Wang, Q. Peng, L. Gu, X. Han, J. Li and Y. Li, *Nat. Nanotechnol.*, 2018, **13**, 856-861.
22. Y. He, J.-C. Liu, L. Luo, Y.-G. Wang, J. Zhu, Y. Du, J. Li, S. X. Mao and C. Wang, *Proc. Natl. Acad. Sci. U. S. A.*, 2018, **115**, 7700-7705.
23. J. Jones, H. Xiong, A. T. DeLaRiva, E. J. Peterson, H. Pham, S. R. Challa, G. Qi, S. Oh, M. H. Wiebenga, X. I. Pereira Hernández, Y. Wang and A. K. Datye, *Science*, 2016, **353**, 150-154.
24. F. Dvořák, M. Farnesi Camellone, A. Tovt, N.-D. Tran, F. R. Negreiros, M. Vorokhta, T. Skála, I. Matolínová, J. Mysliveček, V. Matolín and S. Fabris, *Nat. Commun.*, 2016, **7**, 10801.
25. L. Nie, D. Mei, H. Xiong, B. Peng, Z. Ren, X. I. P. Hernandez, A. DeLaRiva, M. Wang, M. H. Engelhard, L. Kovarik, A. K. Datye and Y. Wang, *Science*, 2017, **358**, 1419-1423.
26. D. Kunwar, S. Zhou, A. DeLaRiva, E. J. Peterson, H. Xiong, X. I. Pereira-Hernández, S. C. Purdy, R. ter Veen, H. H. Brongersma, J. T. Miller, H. Hashiguchi, L. Kovarik, S. Lin, H. Guo, Y. Wang and A. K. Datye, *ACS Catal.*, 2019, **9**, 3978-3990.
27. R. Lang, W. Xi, J.-C. Liu, Y.-T. Cui, T. Li, A. F. Lee, F. Chen, Y. Chen, L. Li, L. Li, J. Lin, S. Miao, X. Liu, A.-Q. Wang, X. Wang, J. Luo, B. Qiao, J. Li and T. Zhang, *Nat. Commun.*, 2019, **10**, 234.
28. I. Ro, M. Xu, G. W. Graham, X. Pan and P. Christopher, *ACS Catal.*, 2019, **9**, 10899-10912.
29. L. DeRita, J. Resasco, S. Dai, A. Boubnov, H. V. Thang, A. S. Hoffman, I. Ro, G. W. Graham, S. R. Bare, G. Pacchioni, X. Pan and P. Christopher, *Nat. Mater.*, 2019, **18**, 746-751.
30. G. Spezzati, Y. Su, J. P. Hofmann, A. D. Benavidez, A. T. DeLaRiva, J. McCabe, A. K. Datye and E. J. M. Hensen, *ACS Catal.*, 2017, **7**, 6887-6891.
31. H. Jeong, D. Shin, B.-S. Kim, J. Bae, S. Shin, C. Choe, J. W. Han and H. Lee, *Angew. Chem. Int. Ed.*, 2020, **59**, 20691-20696.
32. H. Wang, J.-X. Liu, L. F. Allard, S. Lee, J. Liu, H. Li, J. Wang, J. Wang, S. H. Oh, W. Li, M. Flytzani-Stephanopoulos, M. Shen, B. R. Goldsmith and M. Yang, *Nat. Commun.*, 2019, **10**, 3808.
33. M. Inomata, K. Mori, A. Miyamoto, T. Ui and Y. Murakami, *The Journal of Physical Chemistry*, 1983, **87**, 754-761.
34. I. E. Wachs, *Dalton Transactions*, 2013, **42**, 11762-11769.
35. H. Y. Kim, H. M. Lee, R. G. S. Pala and H. Metiu, *J. Phys. Chem. C*, 2009, **113**, 16083-16093.
36. G. Deo and I. E. Wachs, *J. Catal.*, 1994, **146**, 323-334.
37. I. E. Wachs, *Catal. Today*, 1996, **27**, 437-455.
38. F. Yang, S. Kundu, A. B. Vidal, J. Graciani, P. J. Ramírez, S. D. Senanayake, D. Stacchiola, J. Evans, P. Liu, J. F. Sanz and J. A. Rodriguez, *Angew. Chem. Int. Ed.*, 2011, **50**, 10198-10202.
39. J. Resasco and P. Christopher, *J. Phys. Chem. Lett.*, 2020, **11**, 10114-10123.
40. K. Ding, A. Gulec, A. M. Johnson, N. M. Schweitzer, G. D. Stucky, L. D. Marks and P. C. Stair, *Science*, 2015, **350**, 189-192.
41. E. D. Goodman, A. C. Johnston-Peck, E. M. Dietze, C. J. Wrasman, A. S. Hoffman, F. Abild-Pedersen, S. R. Bare, P. N. Plessow and M. Cargnello, *Nat. Catal.*, 2019, **2**, 748-755.
42. L. Liu, D. M. Meira, R. Arenal, P. Concepcion, A. V. Puga and A. Corma, *ACS Catal.*, 2019, **9**, 10626-10639.
43. C. Dessal, T. Len, F. Morfin, J.-L. Rousset, M. Aouine, P. Afanasiev and L. Piccolo, *ACS Catal.*, 2019, **9**, 5752-5759.
44. H. Y. Kim and G. Henkelman, *J. Phys. Chem. Lett.*, 2013, **4**, 216-221.
45. H. Ha, S. Yoon, K. An and H. Y. Kim, *ACS Catal.*, 2018, **8**, 11491-11501.
46. Y. Choi, S. K. Cha, H. Ha, S. Lee, H. K. Seo, J. Y. Lee, H. Y. Kim, S. O. Kim and W. Jung, *Nat. Nanotechnol.*, 2019, **14**, 245-251.
47. K. Mudiyanselage, H. Y. Kim, S. D. Senanayake, A. E. Baber, P. Liu and D. Stacchiola, *Physical Chemistry Chemical Physics*, 2013, **15**, 15856-15862.
48. D. Yan, J. Chen and H. Jia, *Angew. Chem. Int. Ed.*, 2020, **59**, 13562-13567.
49. R. Lang, X. Du, Y. Huang, X. Jiang, Q. Zhang, Y. Guo, K. Liu, B. Qiao, A. Wang and T. Zhang, *Chem. Rev.*, 2020, **120**, 11986-12043.
50. X. I. Pereira-Hernández, A. DeLaRiva, V. Muravev, D. Kunwar, H. Xiong, B. Sudduth, M. Engelhard, L. Kovarik, E. J. M. Hensen, Y. Wang and A. K. Datye, *Nat. Commun.*, 2019, **10**, 1358.
51. H. Y. Kim, M. S. Hybertsen and P. Liu, *Nano Lett.*, 2017, **17**, 348-354.
52. L. DeRita, S. Dai, K. Lopez-Zepeda, N. Pham, G. W. Graham, X. Pan and P. Christopher, *J. Am. Chem. Soc.*, 2017, **139**, 14150-14165.
53. X. Li, X. Yang, J. Zhang, Y. Huang and B. Liu, *ACS Catal.*, 2019, **9**, 2521-2531.
54. E. Paparazzo, G. M. Ingo and N. Zacchetti, *Journal of Vacuum Science & Technology A*, 1991, **9**, 1416-1420.

This journal is © The Royal Society of Chemistry 20xx

Please do not adjust margins